ELECTROCHEMISTRY

Partially exposed RuP₂ surface in hybrid structure endows its bifunctionality for hydrazine oxidation and hydrogen evolution catalysis

Yapeng Li[1]*, Jihua Zhang[2]*, Yi Liu[1], Qizhu Qian[1], Ziyun Li[1], Yin Zhu[3], Genqiang Zhang[1]†

Replacing the sluggish anode reaction in water electrolysis with thermodynamically favorable hydrazine oxidation could achieve energy-efficient H_2 production, while the shortage of bifunctional catalysts limits its scale development. Here, we presented the scalable one-pot synthesis of partially exposed RuP_2 nanoparticle–decorated carbon porous microsheets, which can act as the superior bifunctional catalyst outperforming Pt/C for both hydrazine oxidation reaction and hydrogen evolution reaction, where an ultralow working potential of −70 mV and an ultrasmall overpotential of 24 mV for 10 mA cm^{-2} can be achieved. The two-electrode electrolyzer can reach 10 mA cm^{-2} with a record-low cell voltage of 23 mV and an ultrahigh current density of 522 mA cm^{-2} at 1.0 V. The DFT calculations unravel the notability of partial exposure in the hybrid structure, as the exposed Ru atoms are the active sites for hydrazine dehydrogenation, while the C atoms exhibit a more thermoneutral value for H* adsorption.

INTRODUCTION

High-purity hydrogen (H_2) production based on water electrolysis has been considered as an eco-friendly and carbon-neutral strategy compared to traditional solutions such as steam reforming and coal gasification, which could promote the advance of future hydrogen economy society (1–3). However, the intrinsically sluggish kinetics of oxygen evolution reaction [OER; $4OH^- = O_2 + 2H_2O + 4e^-$, 1.23 V versus reversible hydrogen electrode (RHE)] is deemed as the bottleneck for the future development of hydrogen economy (4), although a variety of extraordinary electrocatalysts have been developed (5–7). In this context, replacing anodic OER with small-molecule oxidation reactions having favorable thermodynamic potential has recently been proposed to achieve energy-saving H_2 production (8, 9). Some pioneering works have demonstrated the viability by using hydrazine oxidation reaction (HzOR; $N_2H_4 + 4OH^- = N_2 + 4H_2O$, −0.33 V versus RHE) at the anode side to drive overall hydrazine splitting (OHzS) to obtain H_2 at a much lower cell voltage (10, 11), which has cut a notable figure as a kind of hybrid water splitting. For example, Sun et al. (12) reported that Fe doped CoS_2 nanosheets have effective HzOR activity and could achieve the current density of 10 mA cm^{-2} at about −5 mV versus RHE, nearly 1.5 V lower than that of the corresponding water oxidation with the recently reported dominant materials (13, 14). Despite these leading achievements, it is still at the infant stage where key challenges remained. The first problem is that the HzOR performance of the present materials is unsatisfactory, as the working potential is far higher than the theoretical value. Another prominent challenge is the exploitation of high-performance bifunctional catalysts toward both HzOR and hydrogen evolution reaction (HER), which is quite difficult since the active species for each catalytic process are generally different, thus raising tougher requirements on smart and precise materials design strategies. In

addition, the investigation on the H_2 production system based on sole liquid fuel is underdeveloped, where concentrated focus should be devoted to pushing forward the advance of practical applications.

Recently, noble metal phosphide (NMP)–based hybrid structures have gained a lot of attention due to their comparable HER activity to the state-of-the-art Pt/C but much lower noble metal dosage (15). For example, Mu et al. (16) reported the fabrication of an ultrathin N-doped carbon (NC) encapsulated IrP_2 (IrP_2@NC) electrocatalyst with superior activity for HER achieving ultralow overpotential of 28 mV at 10 mA cm^{-2} in 1.0 M KOH, which may attribute to the modulated C active sites in NC layer activated by IrP_2 core. However, just as a coin has two sides, the carbon layer that is active for HER generally has unsatisfactory activity for HzOR catalysis since the metal sites in the composite are frequently identified as the active sites in most cases (17). As a consequence, it is reasonable to deduce that designing a hybrid structure of carbon-based substrate coupled with partially exposed NMP nanoparticles could generate bifunctional surfaces, i.e., active C sites for HER and exposed metal sites for HzOR, yet has been rarely referred in previous literatures.

Here, we present a rationally designed synthesis of partially exposed RuP_2 nanoparticle–decorated N, P dual-doped carbon porous microsheets (denoted as RP-CPM) using a scalable one-pot strategy, which outperforms benchmark Pt/C toward both hydrazine oxidation and hydrogen evolution in alkaline condition. Specifically, it only requires an ultrasmall working potential of −70 mV to reach 10 mA cm^{-2} for HzOR [131 mV for 20 weight % (wt %) Pt/C] in 1.0 M KOH/0.3 M N_2H_4 and an extremely low overpotential of 24 mV at 10 mA cm^{-2} for HER (35 mV for 20 wt % Pt/C) in 1.0 M KOH. Outstandingly, a record-low cell voltage of 23 mV is needed to obtain 10 mA cm^{-2} in a two-electrode system for OHzS (166 mV for 20 wt % Pt/C), and an ultrahigh current density of 522 mA cm^{-2} can be reached at a small cell voltage of 1.0 V. Furthermore, we demonstrated an extended application of RP-CPM as anode catalyst in direct hydrazine fuel cell (DHzFC), where a decent power density of 64.77 mW cm^{-2} can be achieved in 1.0 M KOH/0.5 M N_2H_4 electrolyte at room temperature. Benefitting from the outstanding performance, the H_2 production system with hydrazine as sole liquid fuel is then demonstrated through the DHzFC-powered OHzS, where a promising H_2 generation rate of 0.68 mmol hour^{-1} can be

[1]Hefei National Laboratory for Physical Sciences at the Microscale, CAS Key Laboratory of Materials for Energy Conversion, and Department of Materials Science and Engineering, University of Science and Technology of China, Hefei 230026, Anhui, China. [2]Guizhou Provincial Key Laboratory of Computational Nano-Material Science, Guizhou Education University, Guiyang 550018, Guizhou, China. [3]Department of Chemistry, University of Science and Technology of China, Hefei 230026, Anhui, China.
*These authors contributed equally to this work.
†Corresponding author. Email: gqzhangmse@ustc.edu.cn

achieved at room temperature with a relatively low hydrazine addition (0.5 M for DHzFC and 0.3 M for OHzS). The density functional theory (DFT) calculations decipher that the C sites in RP-CPM exhibit more thermoneutral hydrogen absorption kinetics for HER, while the active Ru sites in the hybrid structure have more favorable dehydrogenation kinetics compared to that of pure RuP_2 for HzOR, demonstrating the significance of the partially exposed RuP_2 surface.

RESULTS

Synthesis and characterization of RP-CPM catalyst

The synthesis procedure is schematically illustrated in Fig. 1A, which is extremely simple and scalable. The Ru-MP precursor is first obtained by mixing a certain amount of MP and $RuCl_3$ in ethanol since the abundant amino group could promote the absorption of Ru^{3+} through the electrostatic interaction. The final RP-CPM can then be formed via thermal annealing treatment of Ru-MP precursor at 850°C under Ar atmosphere. The morphological information of the RP-CPM is observed by field-emission scanning electron microscopy (FESEM) and transmission electron microscopy (TEM).

The typical FESEM image (Fig. 1B) shows that the RP-CPM exhibits porous microsheet morphology, and the TEM image (Fig. 1C) clearly indicates that the microsheets are decorated with isolated nanoparticles with average diameters of about 12 nm (fig. S1). The associated x-ray diffraction (XRD) pattern of RP-CPM (Fig. 1D) can be well indexed to the orthorhombic RuP_2 phase [Joint Committee on Powder Diffraction Standards (JCPDS) no. 34-0333]. The high-resolution TEM (HRTEM) analysis (Fig. 1E) reveals that the decorated RuP_2 nanoparticles are not conformally coated with carbon shells, as almost every single nanoparticle has partially exposed surface labeled with yellow dotted lines. This partial exposure feature broadly exists in the RP-CPM hybrid structure (fig. S2), which is unique compared with fully covered metal phosphide architecture that existed in most previous literatures (18–20), and may imply its unique electrocatalytic activity. The clear lattice fringes (Fig. 1F) indicate the good crystallinity and the interplanar spacing of 3.87 and 2.30 Å corresponding to the (110) and (111) planes of RuP_2, respectively. Meanwhile, the Raman spectrum (Fig. 1G) gives an obvious signal of D and G band from carbon besides the characteristic P—P bond from the RuP_2 phase (see note S1 for details), suggesting the formation of hybrid
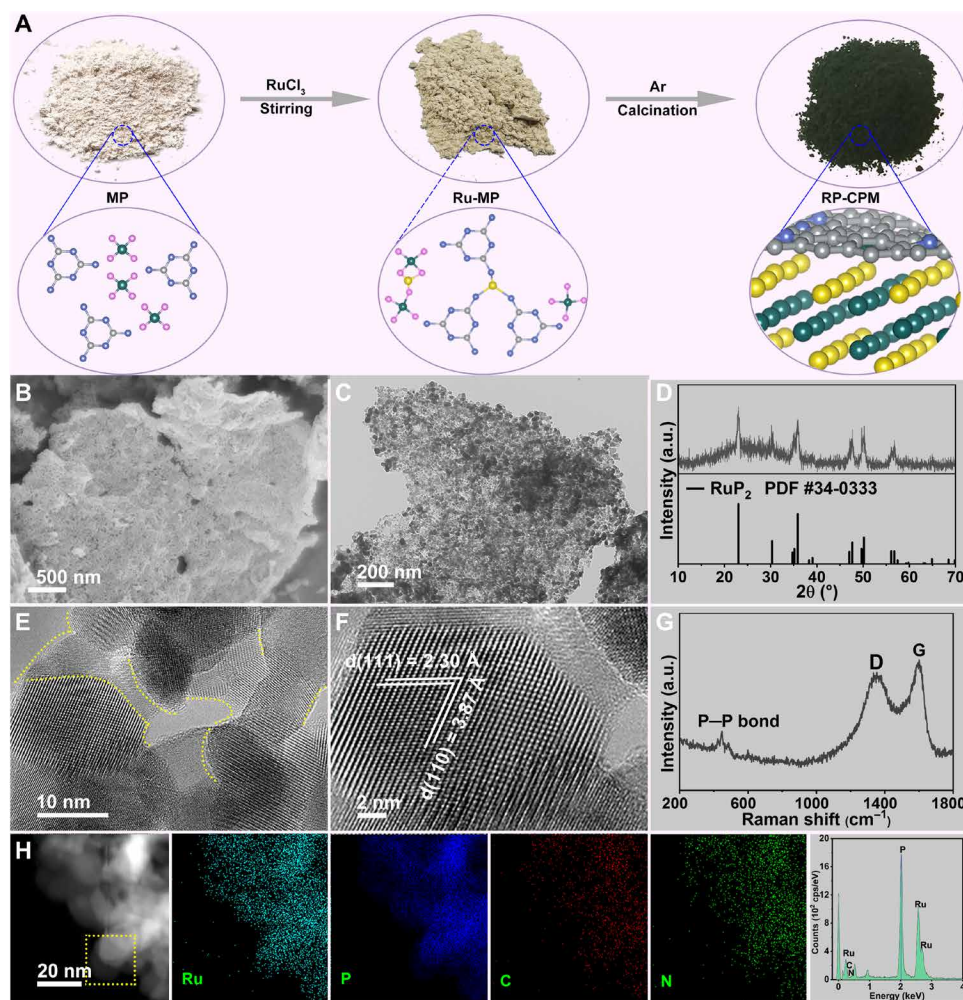

Fig. 1. The formation process and morphological and structural characterizations for RP-CPM. (**A**) Schematic illustration. Photo credit: Yapeng Li, University of Science and Technology of China. (**B** and **C**) FESEM and TEM images. (**D**) XRD pattern. a.u., arbitrary units. (**E** and **F**) HRTEM analysis. (**G**) Raman spectrum. a.u., arbitrary units. (**H**) STEM-HAADF image, the corresponding elemental mapping results, and the energy dispersive spectroscopy (EDS) spectrum of the rectangular region marked with yellow dotted line.

structure composed of RuP$_2$ and graphitized carbon. To further confirm the partial exposure feature, the high-angle annular dark-field scanning TEM (HAADF-STEM) analysis was further conducted on the edge of RuP$_2$ nanoparticle (Fig. 1H); the result suggests that the nanoparticles are composed of the heavy elements of Ru and P while C and N are sparse. Specifically, the atomic ratio of Ru:P:C:N on an single nanoparticle marked with yellow dotted line in the HAADF-STEM image is about 32.45:63.74:3.81:0, which is different from that of the whole sheet with uniformly distributed C and N throughout the microsheets decorated with nanoparticles composed of Ru and P elements (fig. S3). The above experimental analysis suggests that the exposed nanoparticle is RuP$_2$ (Ru:P = 1:1.96) without the conformal coating of graphene layers. The influence of annealing temperatures on the morphology and structure of the products is also performed, where it can be observed that annealing at 800°C cannot form crystalline RuP$_2$ phase, while higher annealing temperature of 900°C will induce the generation of the agglomerated RuP$_2$ particles in the hybrid structure (fig. S4).

The surface chemical state of RP-CPM is then investigated by x-ray photoelectron spectroscopy (XPS) characterization. The survey spectrum (fig. S5) indicates the existence of C, N, P, and Ru with the atomic content of 91.7, 2.1, 4.3, and 1.9%, respectively. The loading of Ru is about 13.17 wt % and that of RuP$_2$ can then be calculated as 21.29 wt %, which is consistent with the inductively coupled plasma (ICP) results (13.71 wt % for Ru and the atomic ratio of P and Ru is ~2.5). The peaks in the Ru high-resolution spectrum at 461.8 and 484.3 eV (Fig. 2A) can be assigned to the Ru 3p$_{3/2}$ and 3p$_{1/2}$ of RuP$_2$, respectively (21). Figure 2B depicts the deconvoluted doublet peaks situated at 129.3 and 130.0 eV, respectively, which belong to the spin splitting of P in the Ru-P species. The other deconvoluted peak at 133.6 eV can be assigned to the P—C bond, whose binding energy is higher than that of P^0 (130.2 eV), suggesting the doping of P into the C skeleton and the possible charge transfer from P to C (22). The P-O peak located at 134.2 eV may come from surface oxidation of the sample when exposed in the air (23). The C 1s envelope (Fig. 2C) can be deconvoluted to C–N (286.8 eV) and C–P (285.5 eV) peaks, further confirming the incorporation of N and P into the C skeleton (24). The peaks centered at 280.5 and 284.6 eV in the C 1s spectrum belong to the Ru 3d$_{5/2}$ and 3d$_{3/2}$ in the RP-CPM along with the relevant satellite peaks located at 282.5 and 286.3 eV, respectively (25). The positive shift of Ru 3d$_{5/2}$ binding energy than that of Ru metal (279.8 eV) implies that the Ru in RP-CPM could hold a partial positive charge (δ^+) (26). The N 1s high-resolution spectrum in Fig. 2D mainly contains four peaks situated at 398.4 eV (pyridinic N), 400.6 eV (pyrrolic N), 401.8 eV (graphitic N), and 404 eV (oxygenated N), respectively; among those, the high content of graphitic N (39 atomic %) could be favorable for the electrocatalytic activity through modulating the electronic structure (27). The XPS results imply that the unique hybrid structure of partially exposed RuP$_2$ in the carbon matrix may induce the interfacial charge transfer from Ru to P and then to coupled C (22) and thus may modulate the Ru and C simultaneously, which could further improve the bifunctional performance for HzOR and HER.

## Investigation of electrocatalytic HzOR and HER activities

The HzOR and HER performances were examined using a typical three-electrode configuration with Hg/HgO (1.0 M KOH) as the reference electrode (the electrode has been carefully calibrated with RHE, as shown in fig. S6) and graphite rod as the counter electrode
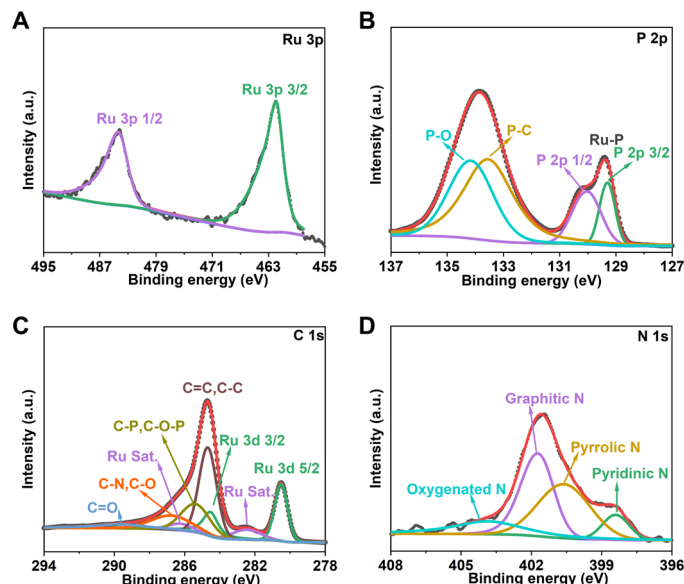
Fig. 2. The investigation on surface chemical states of RP-CPM. (**A**) Ru 3p, (**B**) P 2p, (**C**) C 1s, and (**D**) N 1s high-resolution spectra of RP-CPM. a.u., arbitrary units.

(Φ = 6 mm). The electrochemical performance of the samples at different thermal annealing temperatures was firstly investigated to screen out the optimal samples, where it is obvious that the RP-CPM obtained at 850°C exhibits the best bifunctional activity (fig. S7) and the term RP-CPM means that the sample synthesized at 850°C unless specified. The electrocatalytic HzOR activity of RP-CPM was then evaluated in 1.0 M KOH electrolyte with different N$_2$H$_4$ concentrations. The linear sweep voltammetry (LSV) curves (Fig. 3A) show that there is no oxidation current when the electrolyte is 1.0 M KOH in the measured potential window of −0.1 to 0.7 V (versus RHE). Increasing the N$_2$H$_4$ concentration to 0.1 M, the anodic current shows a sharp rise, which keeps increasing with the N$_2$H$_4$ concentrations changing from 0.1 to 0.3 M, and presents the similar variation tendency with N$_2$H$_4$ concentration increasing from 0.3 to 0.5 M (fig. S8), suggesting the promising catalytic activity of the RP-CPM toward HzOR (28). The current response with ultralow N$_2$H$_4$ concentrations from 0 to 10 mM (fig. S9A) was further investigated in alkaline electrolyte (1.0 M KOH) to explore its possibility for detecting environmental pollutant hydrazine. The relevant calibration curve (fig. S9B) indicates that the oxidation current increases linearly with the added hydrazine and the detection limit based on the signal-to-noise ratio of 3 is evaluated to be 36 μM, suggesting the promising application of RP-CPM as an electrochemical sensor for the detection of hydrazine (10). Besides, the LSV curves have no obvious change at variable scan rates from 10 to 100 mV s^{-1}, as shown in Fig. 3B, implying the efficient charge and mass transport during the catalytic process (29). The electrocatalytic performance of the control samples for HzOR is presented in Fig. 3C, where the pure RuP$_2$ particles (orthorhombic phase, JCPDS no. 34-0333; fig. S10, A to C) were synthesized via the phosphorization of RuCl$_3$ with red P and the CPMs were obtained by the direct thermolysis of MP (fig. S10, D to F). It is worth mentioning that the mixture of RuP and RuP$_2$ can be synthesized at 850°C (fig. S11), while CPM annealed at 850°C has the negligible activity for HzOR and HER (fig. S12) than that obtained at 900°C, mainly because of the poor graphitization (fig. S13). Thus, we choose 900°C as the annealing temperature
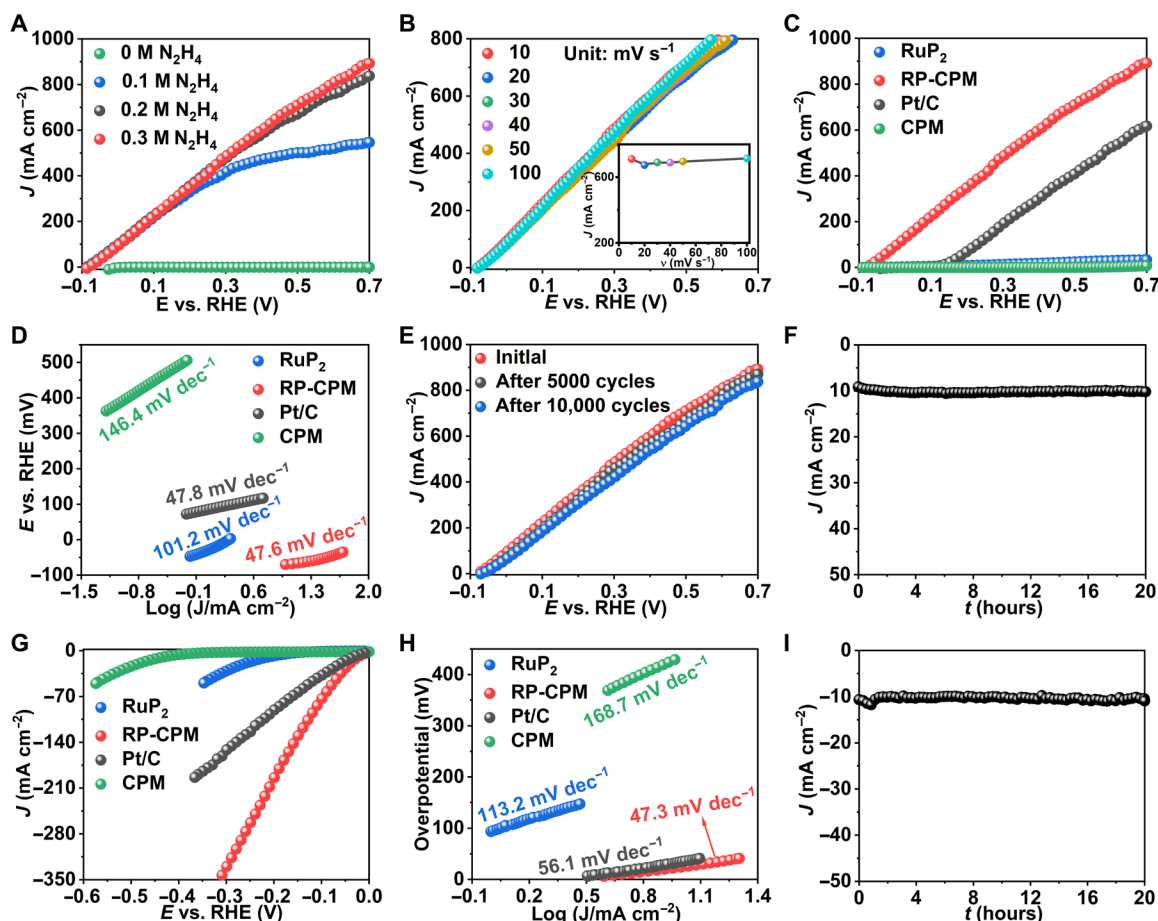
Fig. 3. The study of HzOR and HER for RP-CPM. (**A**) LSV curves of RP-CPM with a scan rate of 5 mV s^{-1} in 1.0 M KOH containing different concentrations of hydrazine. (**B**) LSV curves of RP-CPM with different scan rates. The inset shows the corresponding current density at 0.5 V versus RHE for different scan rates. (**C** and **D**) Polarization curves of RuP$_2$, RP-CPM, Pt/C, and CPM with a scan rate of 5 mV s^{-1} and corresponding Tafel plots. (**E**) LSV curves after different CV circles. (**F**) *I-t* curve at −0.07 V. The solution is 1.0 M KOH containing 0.3 M N$_2$H$_4$. (**G** to **I**) LSV curves at the scan rate of 5 mV s^{-1}, corresponding Tafel plots, and *I-t* plot at the overpotential of 24 mV for RP-CPM catalyst in 1.0 M KOH.

to synthesize the control samples of RuP$_2$ and CPM to make reasonable comparison. The working potential at the current density of 10 mA cm^{-2} for RP-CPM is −70 mV, which is 201 and 306 mV lower than that of Pt/C (131 mV) and RuP$_2$ (236 mV), also outstanding compared with these recent values (see table S1 for the detailed information) (*10, 12*). The huge working potential of 730 mV at 10 mA cm^{-2} for CPM (fig. S12) further indicates the importance of the hybrid structure. Impressively, the RP-CPM only needs 82 and 314 mV to deliver the larger current densities of 200 and 500 mA cm^{-2}, much less than that of Pt/C (308 and 580 mV, respectively). Besides, the corresponding Tafel slope of RP-CPM (Fig. 3D) is 47.6 mV dec^{-1}, which is slightly better than that of benchmark Pt/C (47.8 mV dec^{-1}) and superior compared to those of RuP$_2$ (101.2 mV dec^{-1}) and CPM (146.4 mV dec^{-1}), suggesting the favorable kinetics of RP-CPM for HzOR. The electrochemical impedance spectroscopy analyses are consistent with the above results (fig. S14), where the charge transfer resistance (R_{ct}) of RP-CPM (7.8 ohm) is much lower than those of Pt/C (86.8 ohm), RuP$_2$ (4276.0 ohm), and CPM. The electrochemically active surface areas (ECSAs) of RP-CPM (10.21 cm^2; see fig. S15 and note S2 for the details) is 38 times compared to that of RuP$_2$ (0.26 cm^2) and 8.8 times than that of CPM (1.15 cm^2), implying more exposed active sites of RP-CPM. The slightly higher ECSA of 20 wt % Pt/C (12.56 cm^2) obtained from its

corresponding C_{dl} value (7.11 mF cm^{-2}) may originate from its smaller particle size of Pt (~3.5 nm; fig. S16) than RuP$_2$ in RP-CPM (mean diameter is about 12 nm). Meanwhile, the specific activity normalized by the above ECSA (fig. S17) suggests that the RP-CPM just needs −37 mV to reach the specific current density of 1 mA cm^{-2}, while pure RuP$_2$ and Pt/C require 57 and 190 mV, respectively, and CPM has no obvious oxidation current in the investigated potential window. By further eliminating the influence of ohmic drop (fig. S18), the RP-CPM only needs −75 mV to reach 10 mA cm^{-2} and exhibits much better intrinsic activity (exchange current density, J_0 is 3.61 × 10^{-7} mA cm^{-2}) than that of Pt/C (7.79 × 10^{-10} mA cm^{-2}). The mass activity was further evaluated by normalizing the LSV curves with the mass loading of Ru (13.71 wt %, ICP results) in RP-CPM and Pt (20 wt %) in Pt/C. As shown in fig. S19A, the thriving current density of RP-CPM at the minute working potential than that of Pt/C suggests its remarkable advantage for HzOR. Specifically, RP-CPM can achieve 5 A mg$^{-1}_{Ru}$ at an ultralow potential of 3 mV and exhibit the high mass activity of 18.2 A mg$^{-1}_{Ru}$ at 200 mV (fig. S19B), superior to that of Pt/C (262 mV@5 A mg$^{-1}_{Pt}$ and 2.5 A mg$^{-1}_{Pt}$@200 mV). Next, the durability of RP-CPM was surveyed using accelerated degradation test (ADT). The potential at 10 mA cm^{-2} slightly increases from −70 to −58 mV after 5000 cycles and then to −55 mV after 10,000 cycles, along with the Tafel slope values

slowly increasing from 47.6 to 49.5 mV dec^{-1}, as shown in Fig. 3E and fig. S20. Moreover, almost 100% current density retention (Fig. 3F) can be observed at the working potential of −70 mV during the 20-hour chronoamperometric test, suggesting the excellent long-term stability of RP-CPM catalyst.

The electrochemical performance of RP-CPM for HER was then investigated in 1.0 M KOH. The comparing LSV curves (Fig. 3G) indicate that the RP-CPM merely needs an ultrasmall overpotential of 24 mV to afford the current density of 10 mA cm^{-2}, which outperforms the benchmark Pt/C (35 mV) and is much better than pure RuP$_2$ (214 mV) and CPM (435 mV). The impressive overpotential of 24 mV makes RP-CPM an outstanding candidate for hydrogen catalysis compared to the recently reported literatures about nonprecious and Ru-based electrocatalysts (detailed information provided in table S2) (30). The IR-corrected polarization curves and the extrapolated exchange current density (fig. S21) further confirm the higher activity of the RP-CPM ($\eta_{10} = 21$ mV, $J_0 = 3.07$ mA cm^{-2}) compared to that of commercial Pt/C ($\eta_{10} = 30$ mV, $J_0 = 2.62$ mA cm^{-2}) (31). Besides, the noble metal loading normalized LSV curves (fig. S22) further suggest the better mass activity of RP-CPM ($\eta_{J = 1 A mg^{-1}_{Ru}} = 40$ mV, $J_{\eta = 100 mV} = 3.85$ A mg$^{-1}_{Ru}$) than that of Pt/C ($\eta_{J = 1 A mg^{-1}_{Pt}} = 79$ mV, $J_{\eta = 100 mV} = 1.35$ A mg$^{-1}_{Pt}$), confirming the economic superiority of RP-CPM as HER catalysts. Furthermore, the smaller Tafel slope of 47.3 mV dec^{-1} (Fig. 3H) and minimal R_{ct} (fig. S23) of RP-CPM than those of commercial Pt/C (56.1 mV dec^{-1}), RuP$_2$ (113.2 mV dec^{-1}), and CPM (168.7 mV dec^{-1}) consolidate the profitable kinetics of RP-CPM for hydrogen evolution catalysis. To compare their specific activity, the IR-corrected LSV curves were normalized by the above ECSA. The plot (fig. S24) shows that the ECSA-corrected current density at the overpotential of 100 mV for RP-CPM, Pt/C, RuP$_2$, and CPM is 1.02, 0.26, 0.18, and 0.01 mA cm^{-2}, respectively. This result clearly indicates that RuP$_2$ is not energetically enough and CPM is almost inactive for catalyzing water reduction, while RuP$_2$-modulated C is important for improving the HER activity. In addition, the turnover frequency (TOF) value (fig. S25 and note S3 for the calculation method) of RP-CPM (2.18 s^{-1}) at the overpotential of 100 mV is 1.47 and 3.98 times higher than that of Pt/C (1.46 s^{-1}) and RuP$_2$ (0.55 s^{-1}), indicating the better intrinsic activity of RP-CPM toward HER in alkaline condition. In short, the smaller Tafel slope and R_{ct}, while the higher specific and mass activity, as well as the larger TOF and ECSA, endow RP-CPM with superior HER activity. The accelerated cyclic voltammogram (CV) test of RP-CPM (fig. S26, A and B) shows that the overpotential at 10 mA cm^{-2} exhibits negligible change after 5000 cycles and only decays by 2 mV after 10,000 cycles and the current density at the overpotential of 100 mV slightly decreases from 74 to 70 and then to 66 mA cm^{-2}. Meanwhile, the Tafel slope (fig. S26C) merely fluctuates from the initial 47.3 mV dec^{-1} to the middle 47.8 mV dec^{-1} and then to the last 49.0 mV dec^{-1}. In addition, the long-term durability is further investigated by a chronoamperometric test at the overpotential of 24 mV, where 97.8% current density retention rate can be obtained after 20-hour continuous test (Fig. 3I). These multiple evaluation techniques all confirm the superior activity and outstanding stability of the RP-CPM for HER in alkaline condition.
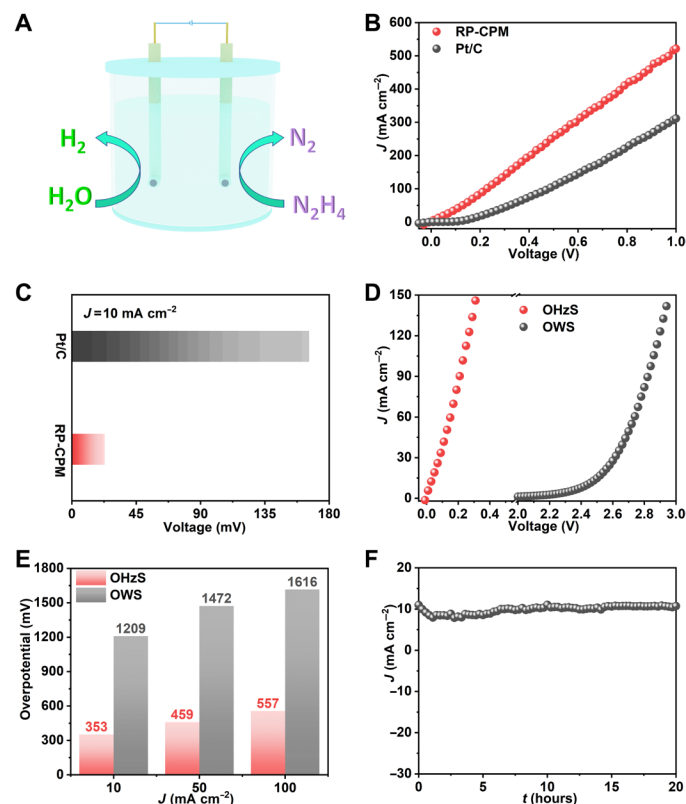
Investigation on the OHzS performance in a two-electrode system

According to the comparing polarization curves (fig. S27A) of RP-CPM and benchmark Pt/C for HER/HzOR couple in 1.0 M KOH/0.3 M N$_2$H$_4$,

it can be observed that the potential gaps to reach 10/100 mA cm^{-2} for RP-CPM are as low as 21/220 mV (fig. S27B), which are 174/244 mV smaller than those of Pt/C, implying its great potential as a bifunctional electrocatalyst for catalyzing H$_2$ generation via OHzS. Notably, the HER behavior in hydrazine-containing alkaline electrolyte is different than that in 1.0 M KOH, where the working potential at 10 mA cm^{-2} shift from −24 to about −90 mV with the increased hydrazine concentrations from 5 to 100 mM (fig. S28). This could be due to the partially overlapped working potential between hydrazine oxidation and hydrogen evolution. Although the HER performance could be disturbed by the addition of N$_2$H$_4$, the ultrasmall potential gap of 21 mV verifies the superior bifunctionality of RP-CPM. Inspired by this, the two-electrode electrolyzers (schematically shown in Fig. 4A) using RP-CPM or commercial Pt/C as both anode and cathode catalysts were fabricated. Considering the safety of mixing anodic N$_2$ with cathodic H$_2$ and the decreased solution resistance, the membrane-free single-chamber cell was selected in our study for OHzS. Their LSV curves (Fig. 4B) can intuitively illustrate the better performance of RP-CPM than that of Pt/C. Specifically, RP-CPM just needs an ultrasmall cell voltage of 23 mV (Fig. 4C) to achieve 10 mA cm^{-2}, much lower than that of Pt/C (166 mV) and remarkable compared to those recently reported values (table S3). Excitingly, it can reach an ultralarge current density of 522 mA cm^{-2} at a cell voltage of 1.0 V, superior among the recent literatures on the energy-saving H$_2$ production systems (32, 33). Besides, the comparing polarization curves (Fig. 4D) of OHzS (1.0 M KOH/0.3 M N$_2$H$_4$) and overall water splitting (OWS; 1.0 M KOH) illustrate the obviously reduced electric power using hydrazine oxidation–assisted H$_2$ production system. Specifically, the hydrazine electrolysis system only needs the cell voltages of 23, 129, and 227 mV to reach 10, 50, and 100 mA cm^{-2} (fig. S29), respectively, while those in the OWS system are 2.439, 2.702, and 2.846 V, respectively. For a comprehensive comparison, the overpotentials (Fig. 4E) for OHzS at the above current densities are 353, 459, and 557 mV, respectively, much smaller than those for OWS systems (1209, 1472, and 1616 mV, respectively). The OHzS system also exhibits outstanding stability (Fig. 4F), where no observable current density decay can be detected during 20-hour electrolysis at an applied cell voltage of 23 mV. The high Faradic efficiency of 99.5% (fig. S30A) can be achieved on the basis of the ratio of experimental and theoretical hydrogen production, which is slightly higher than that of OWS (97.6%; fig. S30B), suggesting the complete electron utilization during hydrogen evolution in the two-electrode system. Note that the widespread applications of hydrazine oxidation are still challenging because of its toxicity and mutagenicity. It has been proposed that fixing hydrazine with carbonyl (>C=O) or amide (—CO—NH$_2$) groups in the harmless, stable, and recyclable polymer to form hydrazone (>C=N—NH$_2$) or hydrazide (—CO—NH—NH$_2$) could be a relatively safe and promising tactic for large-scale applications in the future (34).

The extended application of RP-CPM as anode for DHzFC

The great activity and robust durability of RP-CPM toward HzOR make it promising as an anode catalyst in the DHzFC coupled with Pt/C cathode (Fig. 5A). Unexpectedly, the homemade DHzFC has a high open-circuit voltage of 1.01 V (Fig. 5B) and exhibits a maximum power density of 64.77 mW cm^{-2} at the output voltage of 0.36 V (Fig. 5C) in 1.0 M KOH/0.5 M N$_2$H$_4$ electrolyte working at room temperature, superior than the recently published values under the similar conditions (34, 35). Inspired by the excellent behavior of

Fig. 4. The investigation on the OHzS performance with bifunctional RP-CPM catalyst. (**A**) Schematic illustration of the two-electrode electrolyzer. (**B**) Comparing polarization curves of Pt/C||Pt/C and RP-CPM||RP-CPM couples with a scan rate of 5 mV s^{-1} and (**C**) their corresponding cell voltages at 10 mA cm^{-2}. (**D** and **E**) LSV curves and compared overpotentials of RP-CPM for OWS and OHzS. (**F**) I-t curve for OHzS at the applied cell voltage of 23 mV.

RP-CPM for DHzFC and OHzS, an integrated H$_2$ production system powered by DHzFC based on the sole liquid fuel of hydrazine was demonstrated, as presented in Fig. 5D. The vigorous gas bubble can be observed on both the anode and cathode in the cell (fig. S31 and movie S1) and a decent H$_2$ generation rate of 0.68 mmol hour^{-1} can be achieved (Fig. 5E), which is comparable to the reported values from other self-powered H$_2$ production systems (*36*, *37*), demonstrating its great potential for practical applications.

DISCUSSION
To understand the exceptional electrochemical performance of RP-CPM and investigate the possible structural change, the postcatalytic sample characterizations were executed. The identical XRD patterns and Raman spectra (fig. S32, A and B) between the original and postcatalytic samples suggest the well-retained RuP$_2$ phase and hybrid structure. The TEM images (fig. S32, C and D) show the mostly retained morphology and microstructure, including the porous carbon microsheet and the well-dispersed RuP$_2$ nanoparticles, hence contributing to the structural robustness of the RP-CPM for electrochemical reaction. The Nyquist plots (fig. S33, A and B) show that the R_{ct} has a slight increment after ADTs, suggesting the well-maintained electrode/electrolyte interface and the unaffected charge transfer process under the rigorous electrochemical environment. Besides, the XPS results (fig. S34, A and B) display the unshifted binding energies
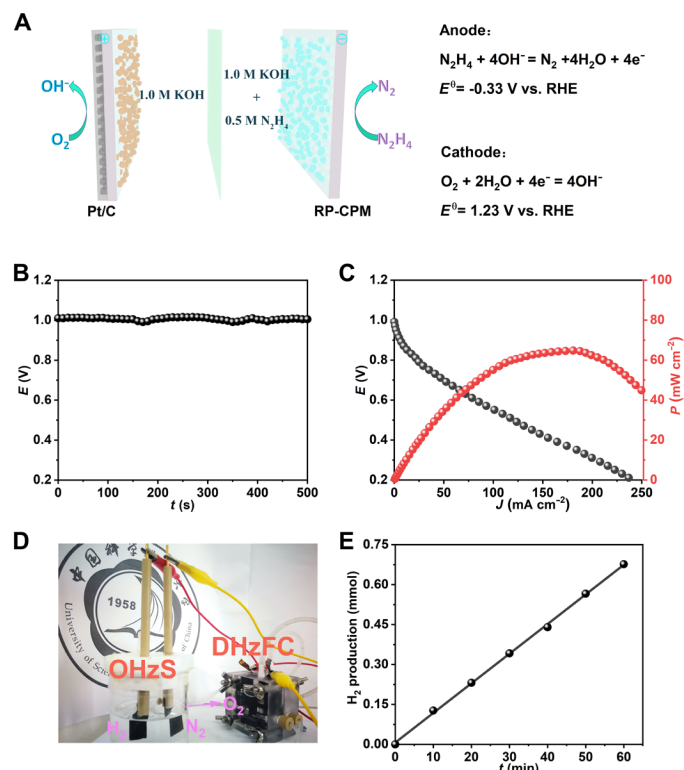

Fig. 5. DHzFC performances of RP-CPM. (**A**) Schematic illustration and working principle of DHzFC. (**B**) Open-circuit voltage of the homemade DHzFC. (**C**) Discharge polarization curve and power density plot of DHzFC. (**D**) Optical image of the integrated H$_2$ production system. Photo credit: Yapeng Li, University of Science and Technology of China. (**E**) Generated amounts of H$_2$ from the integrated H$_2$ production system.

of Ru 3d and P 2p that belong to the Ru-P species and the similar C 1s constituent, suggesting the stable surface chemical states of the RuP$_2$ nanoparticles in the hybrid structure during the electrochemical test. Notably, the P-O peaks in the P 2p spectra of the post-HER/HzOR samples become weaker than that of the as-prepared sample, possibly owing to the dissolution of the phosphate under the test conditions (*38*). The above results imply that the strong coupling between RuP$_2$ nanoparticles and the N, P co-doped CPMs could greatly improve the mechanical strength, could facilitate the electron transfer during the electrochemical process, and thus could be responsible for the enhanced electrochemical activity and durability (*39*). The well-maintained constitution and structure imply that the RP-CPM itself may act as the active species toward both HER and HzOR catalysis.

To reveal the possible origin of RP-CPM's catalytic activity, the DFT calculations were applied to the HzOR and HER process. Optimization results suggest that the Ru-terminated RuP$_2$ (110) surface coupled with two N atoms and one P atom substituted carbon layer are energetically stable (Fig. 6A and fig. S35). It is known that the HER process can be generally described in three steps: an initial catalyst-H$^+$, an intermediate of catalyst-H*, and the final product of 1/2H$_2$, in which the free energy value of adsorbed H (ΔG_{H}*) is the critical descriptor for HER activity (*40*). In this system, it can be calculated that a much more thermoneutral value of 0.04 eV (Fig. 6B) can be obtained for the hybrid structure compared to that for the pure RuP$_2$ (−0.42 eV) and CPM (0.58 eV), suggesting
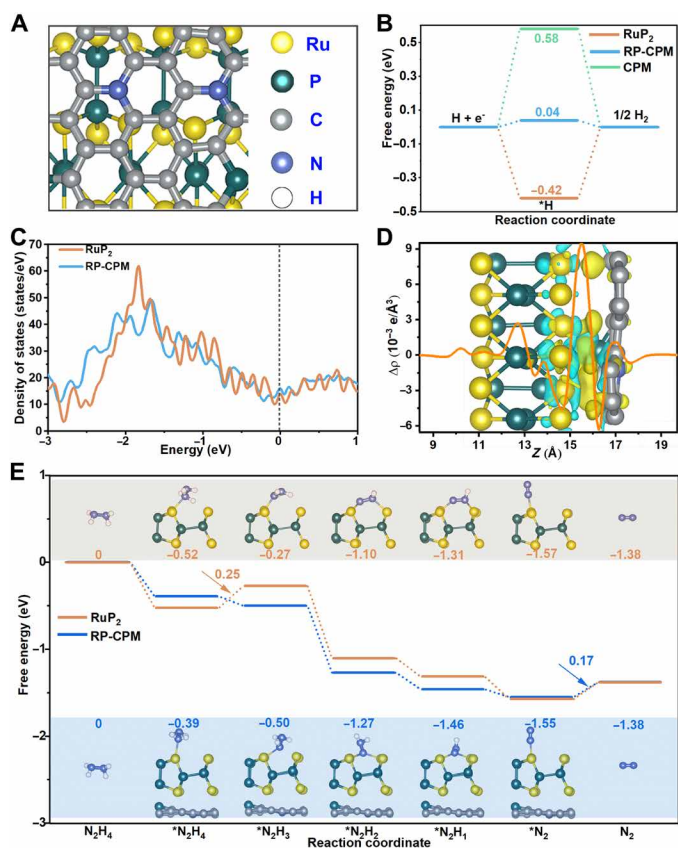
Fig. 6. DFT-relaxed structure models of RP-CPM and the calculated profiles of free energy for HER and HzOR. (**A**) Top-view image of the RP-CPM unit cell. (**B**) Free energy profiles of HER for RP-CPM, RuP$_2$, and CPM. (**C**) Calculated DOS of RuP$_2$ and RP-CPM. (**D**) Charge density difference and planar-averaged electron density difference of RP-CPM. The yellow and cyan colors indicate charge accumulation and depletion, respectively. The isovalues are 0.005 eV/Å^3. (**E**) Reaction pathways and corresponding energy changes of HzOR for RuP$_2$ (top) and RP-CPM (bottom) as well as the free energy profiles of HzOR on the RP-CPM and RuP$_2$ surfaces.

the accelerated hydrogen evolution kinetics on the carbon sites of RP-CPM than the Ru sites of RuP$_2$ (fig. S36), consistent with high HER activity of RP-CPM and the previous report (*41*). The density of states (DOS) and charge density difference for RP-CPM were further calculated. It reveals that the DOS of RP-CPM hybrid structure at the Fermi level is distinctly increased (Fig. 6C), which implies the improved electrical conductivity to boost the charge-transfer kinetics, as well as more charge carriers involved in the catalytic reaction. Figure 6D shows that the charge redistribution of RP-CPM is dominantly restricted on the heterostructure interface and the charge transfers from RuP$_2$ to the carbon layer, which could potentially enhance the catalytic activity of RP-CPM. The markedly decreased water contact angle of hybrid RP-CPM than that of CPM (fig. S37) may be derived from the modification of hydrophilic RuP$_2$, thus further facilitating the penetration of the electrolyte and accelerating the diffusion and transport of active species.

Considering the limited reports on the HzOR activity for RuP$_2$-based catalysts, it is then more meaningful to decipher the fundamental origins of RP-CPM via DFT calculations. First, the possible active sites in the RP-CPM hybrid structure were investigated by comparing the adsorption ability of N$_2$H$_4$ molecular on Ru and C sites,

respectively. As indicated in fig. S38, the distance between the N atom in the N$_2$H$_4$ molecule and the nearest neighboring Ru atom is 2.25 Å, while it increases to 3.78 Å between the N and C atoms of RP-CPM, which is quite different than that for HER catalysis, implying that Ru sites could be the active sites for catalyzing hydrazine oxidation. The experimental results (fig. S39 and note S4) also support the theoretic calculation that the RuP$_2$@PNC with much less exposed RuP$_2$ exhibits the inferior HzOR activity (476 mA cm^{-2}@0.7 V) than that of RP-CPM having partial exposed RuP$_2$ nanoparticles (893 mA cm^{-2}@0.7 V). Figure 6E illustrates the stepwise dehydrogenation processes of N$_2$H$_4$ molecule over the active RuP$_2$ (110) surface for both RP-CPM and pure RuP$_2$, as well as the relative free energy profiles from NH$_2$NH$_2$ to N$_2$ (the calculated N—Ru, N—N, and N—H bond lengths for each dehydrogenation step are present in table S4). Specifically, the absorption of N$_2$H$_4$ is exothermic on the surface of both RP-CPM (−0.39 eV) and RuP$_2$ (−0.52 eV, fig. S40), suggesting that the first absorption process is thermodynamically spontaneous on Ru sites. The large distance (3.57 Å) between the N atom in the N$_2$H$_4$ and the nearest neighboring C atom (fig. S41) in CPM further suggests that the N$_2$H$_4$ molecule cannot be adsorbed on C sites effectively, consistent with the experimental phenomenon. Next, the dehydrogenation from *NH$_2$NH$_2$ to *NHNH$_2$ on the surface of RP-CPM is exothermic successively by −0.11 eV while endothermic by 0.25 eV on that of RuP$_2$, indicating that hybrid structure is easier to accelerate the dissociation of the first H atom from *NH$_2$NH$_2$. Furthermore, the calculation results propose that the desorption of *N$_2$ to N$_2$ is the rate-determining step (RDS) on the surface of RP-CPM, which needs the energy of 0.17 eV. The activation energy of RP-CPM is 0.08 eV smaller than that of RuP$_2$ (0.25 eV), suggesting that the hybrid is more effective to fulfill the multistep dehydrogenation reaction, accounting for the superior electrocatalytic activity for hydrazine oxidation. To validate the dual active sites, i.e., C sites for HER and Ru sites for HzOR, the models with different layers of RuP$_2$ in the hybrid have been selected to theoretically explore the possible influence on HER and HzOR. As indicated, the ΔG$_H$* values for the models with 6, 11, and 16 layers of RuP$_2$ are 0.04, 0.07, and 0.06 eV (fig. S42), respectively, suggesting that the number of RuP$_2$ atom layers has no obvious influence on the HER process. As for HzOR, the model with 16 layers of RuP$_2$ in RP-CPM (fig. S43) results in a much higher ΔG value of 0.34 eV with the RDS from *N$_2$ to N$_2$. In the case of pure RuP$_2$, the model with 16 layers of RuP$_2$ also exhibits higher ΔG value (0.31 eV) and varied RDS from *NH$_2$NH$_2$-*NHNH$_2$ to *N$_2$-N$_2$ compared to that with 6 layers of RuP$_2$, confirming that the number of RuP$_2$ layers indeed affect the HzOR activity, thus providing the beneficial evidence for the dual active sites. Experimentally, when using SCN$^-$ to block the exposed Ru sites in the hybrid, the attenuation of HER activity is step-down while the HzOR performance can be extremely suppressed (fig. S44), further supporting the theoretical calculation results well. These results demonstrate that the unique structure of the partially exposed RuP$_2$ coupled with heteroatom doped CPMs is critical to satisfy the requirement of bifunctional activity for both HzOR and HER. As the C and Ru atoms could be synergistically modulated via the interfacial charge transfer, the kinetic behavior could be facilitated to be more advantageous for both hydrogen adsorption during HER and dehydrogenation process toward HzOR.

In summary, we have achieved the designed synthesis of partially exposed RP-CPM via simple one-pot pyrolysis of small organic

molecules absorbed with Ru species, which exhibits record-high bifunctional electrocatalytic activity for both HzOR and HER in alkaline condition. Concretely, it can reach the current density of 10 mA cm^{-2} at an ultralow working potential of −70 mV for HzOR in 1.0 M KOH/0.3 M N$_2$H$_4$ and just needs an ultrasmall overpotential of 24 mV for HER in 1.0 M KOH, respectively. Remarkably, the OHzS system using RP-CPM as both anode and cathode catalysts only requires an ultrasmall cell voltage of 23 mV to reach the distinct hydrogen generation (10 mA cm^{-2}) and obtain the ultrahigh current density of 522 mA cm^{-2} at the small voltage of 1.0 V. Inspired by the outstanding bifunctional performance, the H$_2$ production system with hydrazine as sole liquid fuel was demonstrated by using the homemade DHzFC as the power source to drive OHzS unit. Furthermore, theory calculation highlights the significance of the partially exposed RuP$_2$ structure in RP-CPM, as the hydrogen absorption on C active sites makes a more thermoneutral value of 0.04 eV for HER process, while the hydrazine dehydrogenation process on active Ru sites is more favorable for HzOR.

MATERIALS AND METHODS

Chemical and materials
Ruthenium(III) chloride anhydrous (RuCl$_3$) and melamine phosphate (MP) were purchased from Aladdin Industrial Corporation. The 5% Nafion solution and Nafion 115 membrane were provided by Sigma-Aldrich Corporation. The commercial 20% Pt/C was provided by Hesen Corporation.

Synthesis of RP-CPM
MP (1.5 mmol) and RuCl$_3$ aqueous solution (1 ml; 0.1 M) were uniformly dispersed in ethanol and stirred for 30 min. Then, a yellowish product (Ru-MP) was obtained and harvested by centrifugation, followed by vacuum-drying overnight. Furthermore, the Ru-MP can be easily transformed to the final product (RP-CPM) via a one-pot pyrolysis at 850°C for 2 hours with a heating rate of 2°C min^{-1} under Ar atmosphere.

Synthesis of RuP$_2$
RuP$_2$ was synthesized via the phosphorization of the commercial RuCl$_3$ with red P at 900°C with a weight ratio of 1:2 in the same atmosphere.

Synthesis of CPM
CPM was synthesized by directly pyrolyzing the MP at 900°C for 2 hours with a heating rate of 2°C min^{-1} under Ar atmosphere.

Synthesis of RuP$_2$@PNC
The preparation was similar to that of the above RP-CPM besides additional o-phenylenediamine (7.5 mmol) being added in the ethanol.

Characterizations
FESEM (SU-8220) and TEM (Hitachi HT7700; Talos F200X; JEM-ARM200F) were used to observe the morphology, lattice fringe, and element distribution. Powder XRD (TTR-III) and Raman spectrometry (Renishaw inVia) with a 532-nm excitation laser were carried out to investigate the phase and graphitization degree. XPS (ESCALAB 250) was applied to analyze the surface element and chemical valence. Attension Theta (Biolin Scientific) was used to measure contact angle. Gas chromatography (GC 7900) equipped with a thermal conductivity detector and TDX-01 column was used to detect the generated gas sampled with a syringe (SCE syringe).

Electrochemical measurements
The typical three-electrode system with graphite rod as the counter electrode, Hg/HgO (1.0 M KOH) as the reference electrode, and glassy carbon (GC) electrode (Φ = 3 mm, L-type) as the substrate of working electrode were used for electrochemical measurements on an electrochemical workstation (CH Instruments 760E) at room temperature. In this study, the reference electrode in our experiment is carefully calibrated with respect to the RHE in high-purity H$_2$-saturated 1.0 M KOH with/without 0.3 M N$_2$H$_4$ aqueous solution with the Pt foils (1 cm by 1 cm) as the working electrode and counter electrode, respectively. The CV curves with the scan rate of 1 mV s^{-1} in the HER/hydrogen oxidation evolution (HOR) region were recorded, and the average value of these two potentials where current cross zero was considered as the thermodynamic potential to the hydrogen electrode reaction.

The apparent current density based on the geometric area of the electrode was the current density indicated in this work unless specified. The GC electrodes were carefully polished before the preparation of working with 500 and 50 nm Al$_2$O$_3$ powders, respectively. Then, 4 μl of catalyst suspension (2.5 mg of catalyst in 1 ml of solution containing 980-μl water/ethanol solution with a volume ratio of 1:1 and 20 μl of 5 wt % Nafion solution) was dropped onto the specular GC surface to give a loading of 0.14 mg cm^{-2} for all samples.
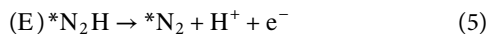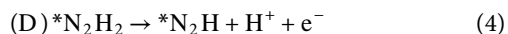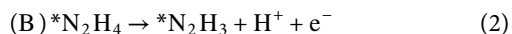
As for the homemade DHzFC, Nafion 115 membrane was used as the proton exchange membrane and RP-CPM loaded on carbon paper (1 cm by 2 cm, 1 mg cm^{-2}, AvCarb MGL190) as anodes and commercial Pt/C (20 wt %) loaded on carbon paper (1 cm by 2 cm, 1 mg cm^{-2}, AvCard GDS3260) with gas diffusion layer as the cathode. When testing the DHzFC, 1.0 M KOH aqueous solution bubbled with O$_2$ as the cathode electrolyte and 1.0 M KOH + 0.5 M N$_2$H$_4$ as the anode electrolyte were flowed into the cell with a flow rate of 1.2 ml min^{-1} by a two-channel peristaltic pump (BT100-2J, Longer Pump) connected with the silicone tube (inner Φ = 3 mm).

Computational details
DFT-based first-principles calculations are performed using the projected augmented wave (42) method implemented in the Vienna Ab initio Simulation Package. The Kohn-Sham one-electron states are expanded using the plane wave basis set with a kinetic energy cutoff of 550 eV. The Perdew-Burke-Ernzerhof (43) exchange-correlation functional within the generalized gradient approximation is used. The Ru-terminated (3 × 1) RuP$_2$ (110) surface slab of six layers is a rectangular cell of 8.567 Å by 7.592 Å, which can nicely matched with 2√3 × 3 unit cell of graphene (8.521 Å by 7.380 Å). For the heterostructures studied in this work, we used the averaged lateral lattice constants (of the supercells) to minimize the strains on both subsystems. The active surface is a Ru-terminated (3 × 1) RuP$_2$ (110) surface. Two of the graphene C atoms are substituted by two N atoms to model the N:graphene/RuP$_2$, while in this N:graphene/RuP$_2$ model, the P atom substitute one of the graphene C to model the NP:graphene/RuP$_2$. The Brillouin zone integration is carried out using the Monkhorst-Pack sampling method with a density of 4 × 4 × 1 for the geometry optimizations. A vacuum layer of 15 Å is included to avoid the interaction between neighboring slabs. All atoms are fully relaxed until the maximum magnitude of the force acting on the atoms is smaller than 0.03 eV/Å.

The oxidation of hydrazine into nitrogen and hydrogen occurs in the following six consecutive elementary steps

$$(A)^* + N_2H_4 \rightarrow {}^*N_2H_4 \qquad (1)$$

$$(B)^*N_2H_4 \rightarrow {}^*N_2H_3 + H^+ + e^- \qquad (2)$$

$$(C)^*N_2H_3 \rightarrow {}^*N_2H_2 + H^+ + e^- \qquad (3)$$

$$(D)^*N_2H_2 \rightarrow {}^*N_2H + H^+ + e^- \qquad (4)$$

$$(E)^*N_2H \rightarrow {}^*N_2 + H^+ + e^- \qquad (5)$$

$$(F)^*N_2 \rightarrow {}^* + N_2 \qquad (6)$$

The asterisk (*) represents the reaction surface of these calculated RuP_2 (110) and NP:graphene/RuP_2. "*N_2H_4," "N_2H_3," "N_2H_2," "N_2H," and "*N_2" denote the models with the corresponding chemisorbed species residing in the reaction surfaces. Among these six elementary steps, steps (A) and (F) are the adsorption of N_2H_4 and desorption of N_2, respectively. The other four elementary steps involve the generation of one proton and one electron. Then, using the computational hydrogen electrode (pH = 0, p = 1 atm, T = 298 K), the Gibbs free energy of $H^+ + e^-$ is replaced implicitly with the Gibbs free energy of one-half a H_2 molecule. Thus, the reaction Gibbs free energies can be calculated using the following equations (44)

$$\Delta G_A = \Delta G_{*N2H4} - \Delta G_* - \Delta G_{N2H4} \qquad (7)$$

$$\Delta G_B = \Delta G_{*N2H3} + 0.5\Delta G_{H2} - \Delta G_{*N2H4} - eU - kT\ln 10 * pH \qquad (8)$$

$$\Delta G_C = \Delta G_{*N2H2} + 0.5\Delta G_{H2} - \Delta G_{*N2H3} - eU - kT\ln 10 * pH \qquad (9)$$

$$\Delta G_D = \Delta G_{*N2H} + 0.5\Delta G_{H2} - \Delta G_{*N2H2} - eU - kT\ln 10 * pH \qquad (10)$$

$$\Delta G_E = \Delta G_{*N2} + 0.5\Delta G_{H2} - \Delta G_{*N2H} - eU - kT\ln 10 * pH \qquad (11)$$

$$\Delta G_F = \Delta G_* + G_{N2} - \Delta G^*_{N2} \qquad (12)$$

U and the pH value in this work are set to zero. The adsorption or reaction Gibbs free energy is defined as: $\Delta G = \Delta E + (\text{ZPE} - T\Delta S)$, where ΔE is the adsorption or reaction energy based on DFT calculations, ΔZPE is the zero point energy (ZPE) correction, T is the temperature, and ΔS is the entropy change. For each system, its ZPE can be calculated by summing vibrational frequencies over all normal modes v (ZPE = $1/2\Sigma h v$). The entropies of gas phase H_2, N_2, and NH_2NH_2 are obtained from the National Institute of Standards and Technology database (45) with the standard condition, and the adsorbed species only took vibrational entropy (Sv) into account, as shown in the following formula

$$Sv = \Sigma_i R\{hv_i/[k_B T * \exp(hv_i/k_B T) - k_B T] - \ln[1 - \exp(-hv_i/k_B T)]\} \qquad (13)$$

Among which, R = 8.314 J mol^{-1} K^{-1}, T = 298.15 K, h = 6.63 × 10^{-34} J·s, k_B = 1.38 × 10^{-23} J K^{-1}, i is the frequency number, and v_i is the vibrational frequency (unit is cm^{-1}).

REFERENCES AND NOTES
1. J. A. Turner, Sustainable hydrogen production. *Science* **305**, 972–974 (2004).
2. S. Chu, A. Majumdar, Opportunities and challenges for a sustainable energy future. *Nature* **488**, 294–303 (2012).
3. Y. Huang, Q. Gong, X. Song, K. Feng, K. Nie, F. Zhao, Y. Wang, M. Zeng, J. Zhong, Y. Li, Mo$_2$C nanoparticles dispersed on hierarchical carbon microflowers for efficient electrocatalytic hydrogen evolution. *ACS Nano* **10**, 11337–11343 (2016).
4. M. W. Kanan, D. G. Nocera, In situ formation of an oxygen-evolving catalyst in neutral water containing phosphate and Co^{2+}. *Science* **321**, 1072–1075 (2008).
5. B. Zhang, X. Zheng, O. Voznyy, R. Comin, M. Bajdich, M. García-Melchor, L. Han, J. Xu, M. Liu, L. Zheng, F. P. García de Arquer, C. T. Dinh, F. Fan, M. Yuan, E. Yassitepe, N. Chen, T. Regier, P. Liu, Y. Li, P. De Luna, A. Janmohamed, H. L. Xin, H. Yang, A. Vojvodic, E. H. Sargent, Homogeneously dispersed multimetal oxygen-evolving catalysts. *Science* **352**, 333–337 (2016).
6. Y. Yao, S. Hu, W. Chen, Z.-Q. Huang, W. Wei, T. Yao, R. Liu, K. Zang, X. Wang, G. Wu, W. Yuan, T. Yuan, B. Zhu, W. Liu, Z. Li, D. He, Z. Xue, Y. Wang, X. Zheng, J. Dong, C.-R. Chang, Y. Chen, X. Hong, J. Luo, S. Wei, W.-X. Li, P. Strasser, Y. Wu, Y. Li, Engineering the electronic structure of single atom Ru sites via compressive strain boosts acidic water oxidation electrocatalysis. *Nat. Catal.* **2**, 304–313 (2019).
7. T. Wang, J. Wu, Y. Liu, X. Cui, P. Ding, J. Deng, C. Zha, E. Coy, Y. Li, Scalable preparation and stabilization of atomic-thick CoNi layered double hydroxide nanosheets for bifunctional oxygen electrocatalysis and rechargeable zinc-air batteries. *Energy Storage Mater.* **16**, 24–30 (2019).
8. Y. Huang, X. Chong, C. Liu, Y. Liang, B. Zhang, Boosting hydrogen production by anodic oxidation of primary amines over a NiSe nanorod electrode. *Angew. Chem. Int. Ed.* **57**, 13163–13166 (2018).
9. B. You, X. Liu, N. Jiang, Y. Sun, A general strategy for decoupled hydrogen production from water splitting by integrating oxidative biomass valorization. *J. Am. Chem. Soc.* **138**, 13639–13646 (2016).
10. C. Tang, R. Zhang, W. Lu, Z. Wang, D. Liu, S. Hao, G. Du, A. M. Asiri, X. Sun, Energy-saving electrolytic hydrogen generation: Ni$_2$P nanoarray as a high-performance non-noble-metal electrocatalyst. *Angew. Chem. Int. Ed.* **56**, 842–846 (2017).
11. J.-Y. Zhang, H. Wang, Y. Tian, Y. Yan, Q. Xue, T. He, H. Liu, C. Wang, Y. Chen, B. Y. Xia, Anodic hydrazine oxidation assists energy-efficient hydrogen evolution over a bifunctional cobalt perselenide nanosheet electrode. *Angew. Chem. Int. Ed.* **57**, 7649–7653 (2018).
12. X. Liu, J. He, S. Zhao, Y. Liu, Z. Zhao, J. Luo, G. Hu, X. Sun, Y. Ding, Self-powered H$_2$ production with bifunctional hydrazine as sole consumable. *Nat. Commun.* **9**, 4365 (2018).
13. L. Bai, C.-S. Hsu, D. T. L. Alexander, H. M. Chen, X. Hu, A cobalt–iron double-atom catalyst for the oxygen evolution reaction. *J. Am. Chem. Soc.* **141**, 14190–14199 (2019).
14. M. Zhao, Z. Chen, Z. Lyu, Z. D. Hood, M. Xie, M. Vara, M. Chi, Y. Xia, Ru octahedral nanocrystals with a face-centered cubic structure, {111} facets, thermal stability up to 400 °C, and enhanced catalytic activity. *J. Am. Chem. Soc.* **141**, 7028–7036 (2019).
15. F. Luo, Q. Zhang, X. Yu, S. Xiao, Y. Ling, H. Hu, L. Guo, Z. Yang, L. Huang, W. Cai, H. Cheng, Palladium phosphide as a stable and efficient electrocatalyst for overall water splitting. *Angew. Chem. Int. Ed.* **57**, 14862–14867 (2018).
16. Z. Pu, J. Zhao, I. S. Amiinu, W. Li, M. Wang, D. He, S. Mu, A universal synthesis strategy for P-rich noble metal diphosphide-based electrocatalysts for the hydrogen evolution reaction. *Energ. Environ. Sci.* **12**, 952–957 (2019).
17. Y. Meng, X. Zou, X. Huang, A. Goswami, Z. Liu, T. Asefa, Polypyrrole-derived nitrogen and oxygen co-doped mesoporous carbons as efficient metal-free electrocatalyst for hydrazine oxidation. *Adv. Mater.* **26**, 6510–6516 (2014).
18. Z. Pu, I. S. Amiinu, Z. Kou, W. Li, S. Mu, RuP$_2$-based catalysts with platinum-like activity and higher durability for the hydrogen evolution reaction at all pH values. *Angew. Chem. Int. Ed.* **56**, 11559–11564 (2017).
19. R. Wang, X.-Y. Dong, J. Du, J. Y. Zhao, S. Q. Zang, MOF-derived bifunctional Cu$_3$P nanoparticles coated by a N, P-codoped carbon shell for hydrogen evolution and oxygen reduction. *Adv. Mater.* **30**, 1703711 (2018).
20. D. Y. Chung, S. W. Jun, G. Yoon, H. Kim, J. M. Yoo, K.-S. Lee, T. Kim, H. Shin, A. K. Sinha, S. G. Kwon, K. Kang, T. Hyeon, Y.-E. Sung, Large-scale synthesis of carbon-shell-coated FeP nanoparticles for robust hydrogen evolution reaction electrocatalyst. *J. Am. Chem. Soc.* **139**, 6669–6674 (2017).

21. Y. Wang, Z. Liu, H. Liu, N. T. Suen, X. Yu, L. Feng, Electrochemical hydrogen evolution reaction efficiently catalyzed by Ru$_2$P nanoparticles. *ChemSusChem* **11**, 2724–2729 (2018).

22. G. Li, Y. Sun, J. Rao, J. Wu, A. Kumar, Q. N. Xu, C. Fu, E. Liu, G. R. Blake, P. Werner, B. Shao, K. Liu, S. Parkin, X. Liu, M. Fahlman, S.-C. Liou, G. Auffermann, J. Zhang, C. Felser, X. Feng, Carbon-tailored semimetal MoP as an efficient hydrogen evolution electrocatalyst in both alkaline and acid media. *Adv. Energy Mater.* **8**, 1801258 (2018).

23. J. Yu, Y. Guo, S. She, S. Miao, M. Ni, W. Zhou, M. Liu, Z. Shao, Bigger is surprisingly better: Agglomerates of larger RuP nanoparticles outperform benchmark Pt nanocatalysts for the hydrogen evolution reaction. *Adv. Mater.* **30**, 1800047 (2018).

24. H. Li, S.-M. Xu, H. Yan, L. Yang, S. Xu, Cobalt phosphide composite encapsulated within N,P-doped carbon nanotubes for synergistic oxygen evolution. *Small* **14**, 1800367 (2018).

25. Z. Guo, J. Li, H. Qi, X. Sun, H. Li, A. G. Tamirat, J. Liu, Y. Wang, L. Wang, A highly reversible long-life Li-CO$_2$ battery with a RuP$_2$-based catalytic cathode. *Small* **15**, 1803246 (2019).

26. D. J. Morgan, Resolving ruthenium: XPS studies of common ruthenium materials. *Surf. Interface Anal.* **47**, 1072–1079 (2015).

27. W. Ye, S. Chen, Y. Lin, L. Yang, S. Chen, X. Zheng, Z. Qi, C. Wang, R. Long, M. Chen, J. Zhu, P. Gao, L. Song, J. Jiang, Y. Xiong, Precisely tuning the number of Fe atoms in clusters on N-doped carbon toward acidic oxygen reduction reaction. *Chem* **5**, 2865–2878 (2019).

28. J.-Y. Zhang, T. He, M. Wang, R. Qi, Y. Yan, Z. Dong, H. Liu, H. Wang, B. Y. Xia, Energy-saving hydrogen production coupling urea oxidation over a bifunctional nickel-molybdenum nanotube array. *Nano Energy* **60**, 894–902 (2019).

29. S. Chen, J. Duan, A. Vasileff, S. Z. Qiao, Size fractionation of two-dimensional sub-nanometer thin manganese dioxide crystals towards superior urea electrocatalytic conversion. *Angew. Chem. Int. Ed.* **55**, 3804–3808 (2016).

30. J. Wang, Z. Wei, S. Mao, H. Li, Y. Wang, Highly uniform Ru nanoparticles over N-doped carbon: pH and temperature-universal hydrogen release from water reduction. *Energ. Environ. Sci.* **11**, 800–806 (2018).

31. Y. Liu, X. Li, Q. Zhang, W. Li, Y. Xie, H. Liu, L. Shang, Z. Liu, Z. Chen, L. Gu, Z. Tang, T. Zhang, S. Lu, A general route to prepare low-ruthenium-content bimetallic electrocatalysts for pH-universal hydrogen evolution reaction by using carbon quantum dots. *Angew. Chem. Int. Ed.* **59**, 1718–1726 (2020).

32. Z.-Y. Yu, C.-C. Lang, M.-R. Gao, Y. Chen, Q.-Q. Fu, Y. Duan, S.-H. Yu, Ni–Mo–O nanorod-derived composite catalysts for efficient alkaline water-to-hydrogen conversion via urea electrolysis. *Energ. Environ. Sci.* **11**, 1890–1897 (2018).

33. Y. Li, X. Wei, L. Chen, J. Shi, M. He, Nickel-molybdenum nitride nanoplate electrocatalysts for concurrent electrolytic hydrogen and formate productions. *Nat. Commun.* **10**, 5335 (2019).

34. K. Asazawa, K. Yamada, H. Tanaka, A. Oka, M. Taniguchi, T. Kobayashi, A platinum-free zero-carbon-emission easy fuelling direct hydrazine fuel cell for vehicles. *Angew. Chem. Int. Ed.* **46**, 8024–8027 (2007).

35. Z. Lu, M. Sun, T. Xu, Y. Li, W. Xu, Z. Chang, Y. Ding, X. Sun, L. Jiang, Superaerophobic electrodes for direct hydrazine fuel cells. *Adv. Mater.* **27**, 2361–2366 (2015).

36. J. Yin, Y. Li, F. Lv, M. Lu, K. Sun, W. Wang, L. Wang, F. Cheng, Y. Li, P. Xi, S. Guo, Oxygen vacancies dominated NiS$_2$/CoS$_2$ interface porous nanowires for portable Zn-air batteries driven water splitting devices. *Adv. Mater.* **29**, 1704681 (2017).

37. J. Zhang, L. Dai, Nitrogen, phosphorus, and fluorine tri-doped graphene as a multifunctional catalyst for self-powered electrochemical water splitting. *Angew. Chem. Int. Ed.* **55**, 13296–13300 (2016).

38. N. Jiang, B. You, M. Sheng, Y. Sun, Electrodeposited cobalt-phosphorous-derived films as competent bifunctional catalysts for overall water splitting. *Angew. Chem. Int. Ed.* **54**, 6251–6254 (2015).

39. J.-S. Li, Y. Wang, C.-H. Liu, S.-L. Li, Y.-G. Wang, L.-Z. Dong, Z.-H. Dai, Y.-F. Li, Y.-Q. Lan, Coupled molybdenum carbide and reduced graphene oxide electrocatalysts for efficient hydrogen evolution. *Nat. Commun.* **7**, 11204 (2016).

40. J. Greeley, T. F. Jaramillo, J. Bonde, I. B. Chorkendorff, J. K. Nørskov, Computational high-throughput screening of electrocatalytic materials for hydrogen evolution. *Nat. Mater.* **5**, 909–913 (2006).

41. Y. Zheng, Y. Jiao, Y. Zhu, L. H. Li, Y. Han, Y. Chen, A. Du, M. Jaroniec, S. Z. Qiao, Hydrogen evolution by a metal-free electrocatalyst. *Nat. Commun.* **5**, 3783 (2014).

42. G. Kresse, D. Joubert, From ultrasoft pseudopotentials to the projector augmented-wave method. *Phys. Rev. B* **59**, 1758–1775 (1999).

43. J. P. Perdew, K. Burke, M. Ernzerhof, Generalized gradient approximation made simple. *Phys. Rev. Lett.* **77**, 3865–3868 (1996).

44. Z. Wang, S.-M. Xu, Y. Xu, L. Tan, X. Wang, Y. Zhao, H. Duan, Y.-F. Song, Single Ru atoms with precise coordination on a monolayer layered double hydroxide for efficient electrooxidation catalysis. *Chem. Sci.* **10**, 378–384 (2019).

45. R. D. Johnson III, *Computational Chemistry Comparison and Benchmark Database* (21 August 2016); http://cccbdb.nist.gov/.

46. Y. Liu, J. Zhang, Y. Li, Q. Qian, Z. Li, Y. Zhu, G. Zhang, Manipulating dehydrogenation kinetics through dual-doping Co$_3$N electrode enables highly efficient hydrazine oxidation assisting self-powered H$_2$ production. *Nat. Commun.* **11**, 1853 (2020).

47. G. Feng, L. An, B. Li, Y. Zuo, J. Song, F. Ning, N. Jiang, X. Cheng, Y. Zhang, D. Xia, Atomically ordered non-precious Co$_3$Ta intermetallic nanoparticles as high-performance catalysts for hydrazine electrooxidation. *Nat. Commun.* **10**, 4514 (2019).

48. Z. Wang, L. Xu, F. Huang, L. Qu, J. Li, K. A. Owusu, Z. Liu, Z. Lin, B. Xiang, X. Liu, K. Zhao, X. Liao, W. Yang, Y.-B. Cheng, L. Mai, Copper–nickel nitride nanosheets as efficient bifunctional catalysts for hydrazine-assisted electrolytic hydrogen production. *Adv. Energy Mater.* **9**, 1900390 (2019).

49. H. Wen, L.-Y. Gan, H.-B. Dai, X.-P. Wen, L.-S. Wu, H. Wu, P. Wang, In situ grown Ni phosphide nanowire array on Ni foam as a high-performance catalyst for hydrazine electrooxidation. *Appl. Catal. B* **241**, 292–298 (2019).

50. N. Jia, Y. Liu, L. Wang, P. Chen, X. Chen, Z. An, Y. Chen, 0.2 V electrolysis voltage-driven alkaline hydrogen production with nitrogen-doped carbon nanobowl-supported ultrafine Rh nanoparticles of 1.4 nm. *ACS Appl. Mater. Interfaces* **11**, 35039–35049 (2019).

51. Q. Sun, M. Zhou, Y. Shen, L. Ma, Y. Li, X. Bo, Z. Wang, C. Zhao, Hierarchical nanoporous Ni(Cu) alloy anchored on amorphous NiFeP as efficient bifunctional electrocatalysts for hydrogen evolution and hydrazine oxidation. *J. Catal.* **373**, 180–189 (2019).

52. G. Liu, Z. Sun, X. Zhang, H. Wang, G. Wang, X. Wu, H. Zhang, H. Zhao, Vapor-phase hydrothermal transformation of a nanosheet array structure Ni(OH)$_2$ into ultrathin Ni$_3$S$_2$ nanosheets on nickel foam for high-efficiency overall water splitting. *J. Mater. Chem. A* **6**, 19201–19209 (2018).

53. Y. Kuang, G. Feng, P. Li, Y. Bi, Y. Li, X. Sun, Single-crystalline ultrathin nickel nanosheets array from in situ topotactic reduction for active and stable electrocatalysis. *Angew. Chem. Int. Ed.* **55**, 693–697 (2016).

54. J. Yu, G. Li, H. Liu, L. Zhao, A. Wang, Z. Liu, H. Li, H. Liu, Y. Hu, W. Zhou, Ru–Ru$_2$PΦNPC and NPC@RuO$_2$ Synthesized via environment-friendly and solid-phase phosphating process by saccharomycetes as N/P sources and carbon template for overall water splitting in acid electrolyte. *Adv. Funct. Mater.* **29**, 1901154 (2019).

55. X. F. Lu, L. Yu, X. W. Lou, Highly crystalline Ni-doped FeP/carbon hollow nanorods as all-pH efficient and durable hydrogen evolving electrocatalysts. *Sci. Adv.* **5**, eaav6009 (2019).

56. Y. Zheng, Y. Jiao, Y. Zhu, L. H. Li, Y. Han, Y. Chen, M. Jaroniec, S.-Z. Qiao, High electrocatalytic hydrogen evolution activity of an anomalous ruthenium catalyst. *J. Am. Chem. Soc.* **138**, 16174–16181 (2016).

57. S. Y. Mar, C. S. Chen, Y. S. Huang, K. K. Tiong, Characterization of RuO$_2$ thin films by Raman spectroscopy. *Appl. Surf. Sci.* **90**, 497–504 (1995).

58. D. E. Bugaris, C. D. Malliakas, D. P. Shoemaker, D. T. Do, D. Y. Chung, S. D. Mahanti, M. G. Kanatzidis, Crystal growth and characterization of the narrow-band-gap semiconductors OsPn$_2$ (Pn = P, As, Sb). *Inorg. Chem.* **53**, 9959–9968 (2014).

59. J. N. Tiwari, A. M. Harzandi, M. Ha, S. Sultan, C. W. Myung, H. J. Park, D. Y. Kim, P. Thangavel, A. N. Singh, P. Sharma, S. S. Chandrasekaran, F. Salehnia, J.-W. Jang, H. S. Shin, Z. Lee, K. S. Kim, High-performance hydrogen evolution by Ru single atoms and nitrided-Ru nanoparticles implanted on N-doped graphitic sheet. *Adv. Energy Mater.* **9**, 1900931 (2019).

60. C. C. McCrory, S. Jung, J. C. Peters, T. F. Jaramillo, Benchmarking heterogeneous electrocatalysts for the oxygen evolution reaction. *J. Am. Chem. Soc.* **135**, 16977–16987 (2013).

61. W. Li, Y. Liu, M. Wu, X. Feng, S. A. Redfern, Y. Shang, X. Yong, T. Feng, K. Wu, Z. Liu, B. Li, Z. Chen, J. S. Tse, S. Lu, B. Yang, Carbon-quantum-dots-loaded ruthenium nanoparticles as an efficient electrocatalyst for hydrogen production in alkaline media. *Adv. Mater.* **30**, 1800676 (2018).